Results in Optics 14 (2024) 100613

Contents lists available at ScienceDirect

Results in Optics

journal homepage: www.sciencedirect.com/journal/results-in-optics

Investigating the effects of varying sulfur concentration on ZnS_xSe_{1-x} ($0 \leq x \leq 1.0$) thin films prepared by photo-assisted chemical bath method

D.D. Hile [a,b,*], H.C. Swart [c], S.V. Motloung [d,e], T.E. Motaung [f], I. Ahemen [a], P.R. Jubu [a], K.E. Essien [g], L.F. Koao [b]

[a] Department of Physics, Joseph Sarwuan Tarka University, Makurdi, Nigeria
[b] Department of Physics, University of the Free State, 9866 Phuthaditjhaba, South Africa
[c] Department of Physics, University of the Free State, ZA9300 Bloemfontein, South Africa
[d] Department of Physical and Chemical Sciences, North-West University (Mafikeng Campus), South Africa
[e] Department of Physics, Sefako Makgatho Health Sciences University, P.O. Box 94, Medunsa 0204, South Africa
[f] Department of Chemistry, School of Science in the College of Science Engineering and Technology, University of South Africa, PO Box 392, UNISA 0003, South Africa
[g] Department of Physics, University of Uyo, Uyo, Nigeria

ARTICLE INFO

Keywords:
Zinc sulfur-selenide
Photo-assisted chemical bath deposition
Thin films
Optical properties

ABSTRACT

Zinc sulfur-selenide (ZnS_xSe_{1-x}) ($0 \leq x \leq 1.0$) thin films were grown on glass substrates using photo-assisted chemical bath deposition technique and the deposited samples were annealed in an open-air furnace at 250 °C for 3 h. X-ray diffraction analysis revealed a phase transition from hexagonal ZnSe to cubic ZnS as x changes from 0 to 1.0. Raman scattering showed two longitudinal optical modes due to ZnSe structure. The effects of S and Se ions variation is observed by the change in surface morphology from nanoflakes to spherical particles as x increased. The presence of the expected elementary composition was confirmed by the energy dispersive x-ray spectroscopy. The bandgap of the films was found to increase from 2.68 to 3.50 eV with a corresponding decrease in crystallite size (11.9 – 7.1 nm) as x varied from 0 to 1.0. Photoluminescence excitation and emission showed defect emission peaks ascribed to intrinsic and extrinsic deep level defects such as Zn^{2+} or S^{2-} ions vacancies and interstitials. The emission colours were tuned from red to yellowish-green with increased x values as confirmed from Commission Internationale de L'Eclairage analysis. The tunability of the ZnS_xSe_{1-x} structural, optical and morphological properties makes it a good candidate for optoelectronic applications.

1. Introduction

The quest for new materials to improve the performance of optoelectronic devices has been an issue of major concern among researchers over the years. Among the materials that are mostly investigated are the binary and ternary II-V I chalcogenide semiconductors compounds such as ZnO (Korepanov et al., 2019), ZnSe (Park et al., 2019), ZnS (Jobzari et al., 2019), CdSe (Olusola et al., 2015), CdTe (Kulkarni et al., 2017), CdS (Echendu et al., 2017). Of the above compounds, zinc base semiconductors have attracted more attention of researchers due to their low toxicity, abundance in the earth's crust and wider bandgap. These materials also possess unique optical, electrical, and thermal properties.

It has been observed that when two semiconductors for example ZnS and ZnSe are combined, the resulting compound formed (ZnSSe) may possess some properties that lie between those of the individual compounds (ZnS and ZnSe) (Patil et al., 2018). Valeev *et al.* (Valeev et al., 2015) in their study of ZnS_xSe_{1-x} thin films synthesized using thermal evaporation method observed that the bandgap was tuned between 2.25 eV (ZnSe) and 3.0 eV (ZnS) when they varied the anionic composition of S and Se in the range $0.36 \leq x \leq 0.73$. It has been reported that ZnSSe compounds have very promising features that could gain them applications in ultraviolet (UV) tunable photodetectors, photo-scintillators, light emitting diodes, UV lasers, and solar cells buffer layers among others (Patil et al., 2018; Valeev et al., 2015; Dimitrievska et al., 2016; Ray et al., 2022). Like many other II-VI compounds, ZnS_xSe_{1-x} thin films semiconductors have been synthesized via different techniques such as spray pyrolysis (Patil et al., 2018), sputtering (Dimitrievska et al., 2016), thermal evaporation (Ray et al., 2022), pulse laser deposition (Lindsey et al., 2016), quassi-closed volume technique (Popa, 2016) and chemical bath deposition (CBD) (Liu

* Corresponding author at: Department of Physics, Joseph Sarwuan Tarka University, Makurdi, Nigeria.
E-mail address: donald.hile@gmail.com (D.D. Hile).

https://doi.org/10.1016/j.rio.2024.100613
Received 12 September 2023; Received in revised form 9 November 2023; Accepted 21 January 2024
Available online 23 January 2024

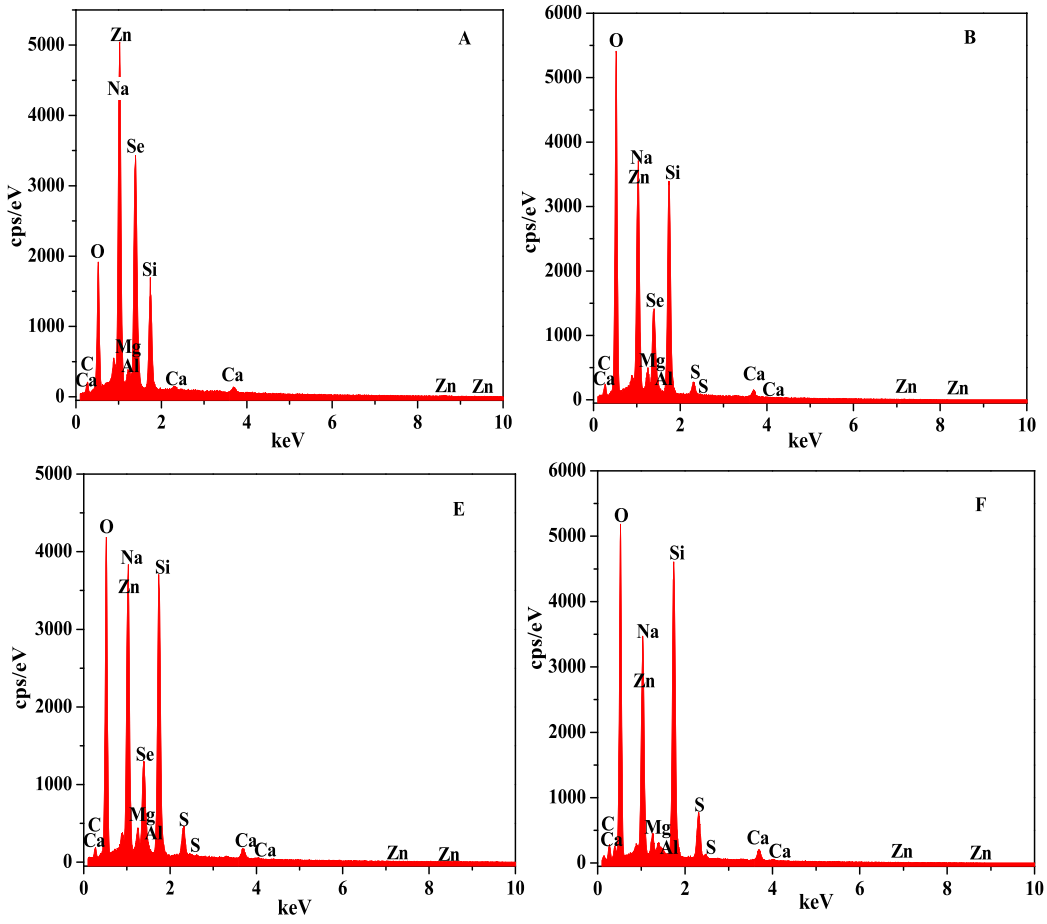

Fig.1. EDX spectra of the selected ZnS_xSe_{1-x} thin films samples.

Table 1
Weight percentages of the elements detected by EDX measurement.

Sample *ID*	Se (Wt%)	Zn (Wt%)	S (Wt%)	O (Wt%)	Si (Wt%)	Na (Wt%)	Ca (Wt%)	Mg (Wt%)	Al (Wt%)	S + Se (Wt%)	*x*
A	36.2	30.9	–	13.8	10.4	5.9	1.4	0.7	0.7	36.2	0
B	13.2	18.3	1.8	32.9	20.8	8.8	1.9	1.7	0.6	15.0	0.12
C	12.2	21.0	3.6	27.9	22.6	8.2	2.4	1.5	0.6	15.8	0.23
D	5.1	13.4	2.2	43.5	22.5	9.4	1.6	1.8	0.5	7.3	0.30
E	2.7	13.6	6.2	35.9	26.3	10.2	3.1	1.6	0.4	8.9	0.70
F	–	14.3	7.4	38.1	25.6	9.8	2.5	1.8	0.5	7.4	1

et al., 2013). CBD is preferred over the other methods because the films are reproducible, the experimental setup is simple, the cost of experimental apparatus is low and large area films can be deposited via this method. Liu *et al.* (Liu et al., 2013) asserted that it is a hard work to obtain pure chalcogenide thin films using CBD. In this present work, a modified CBD known as photo-assisted chemical bath deposition (PCBD) technique is employed for the deposition of ZnS_xSe_{1-x} ($0 \leq x \leq 1.0$) thin films on the non-conducting glass substrate. Some of the advantages of PCBD over CBD include the fact that it produces heterogeneous thin films with a very thin deposit on the vessel, making the solution useful for further depositions (Remadevi et al., 2014). Also PCBD offers efficient conversion of the reactants to the required product, and higher deposition rate (Remadevi and Dhanya, 2011). In our previous study on the comparative analyses of photo- and non-photo-assisted chemical bath deposition of Zinc Selenide thin films using different volumes of hydrazine hydrate (Hile et al., 2019); a higher degree of random distribution of crystallographic orientation was observed in the PCBD samples more than those of the CBD. The thin films morphology was influence by a change in the volume of hydrazine hydrate both with the CBD and the PCBD but the density and agglomeration of the particles were more influenced under the PCBD samples. In the PCBD technique, photo energy is used to facilitate the deposition process mainly as a result of photoexcitation of the solution's molecules. The excited electrons increase the kinetic energy and inter-diffusion of the absorbing particles (Hile et al., 2019). PCBD technique has been employed by other researchers in depositing some binary II-VI chalchogenide compounds such as ThO_2 (Huentupil et al., 2019), SnS (Remadevi et al., 2014), ZnSe (Kumaresan et al., 2002) and ZnS (Remadevi and Dhanya, 2011). However, literature reports on the deposition of tenary compound especially ZnSSe using the PCBD method are rare. The successfully deposited thin films of ZnS_xSe_{1-x} have been subjected to structural, morphological, and optical analyses.

2. Experimental procedure

2.1. Synthesis of ZnS_xSe_{1-x} thin films

The ZnS_xSe_{1-x} thin films were deposited on the clean non-conducting

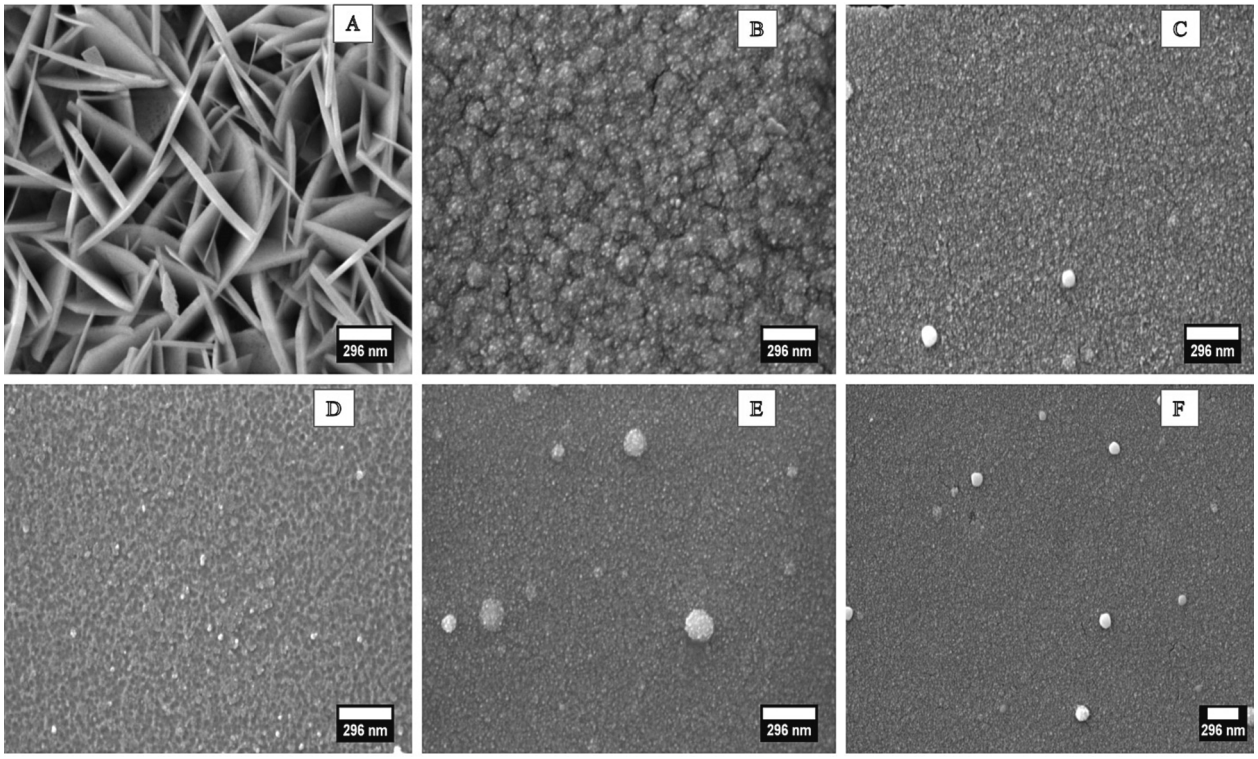

Fig.2. FESEM images of the ZnS_xSe_{1-x} ($0 \leq x \leq 1.0$) thin films.

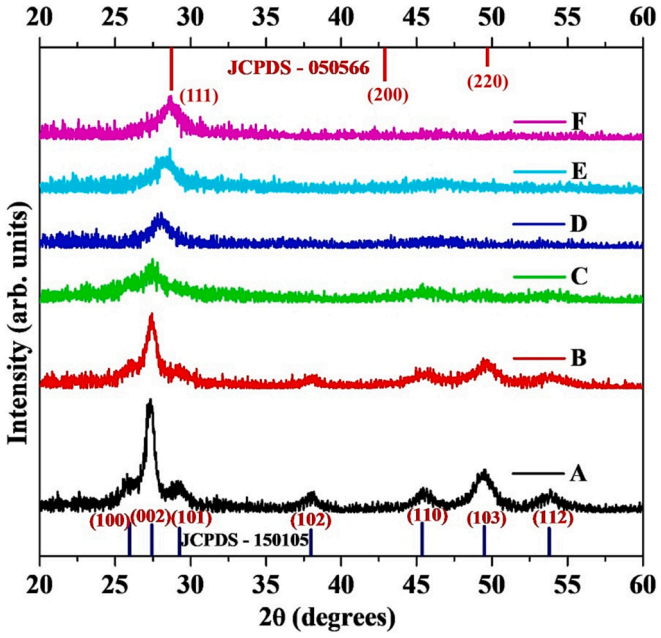

Fig.3. GAXRD patterns of the ZnS_xSe_{1-x} ($0 \leq x \leq 1.0$) thin films.

glass substrates using zinc acetate dehydrate $(CH_3COO)_2Zn{\cdot}2H_2O$ (98 %), hydrazine monohydrate $N_2H_4H_2O$ (80 %), sodium selenosulfate (Na_2SeSO_3) and thiourea CH_4N_2S (98 %) as the precursors. The Na_2SeSO_3 was first prepared from 5 g of Na_2SO_3 (99.9 %) mixed with 1 g selenium powder (≥99.5 %) and 50 mL deionized water. The mixture was refluxed at 80 ℃ for 4 h with constant stirring and a clear and transparent solution was obtained. The deposition of ZnSe was carried out as reported in (Hile et al., 2020) by mixing 20 mL of 0.1 M $(CH_3COO)_2Zn{\cdot}2H_2O$, 20 mL of 80 % $N_2H_4H_2O$, and 20 mL of 0.59 M

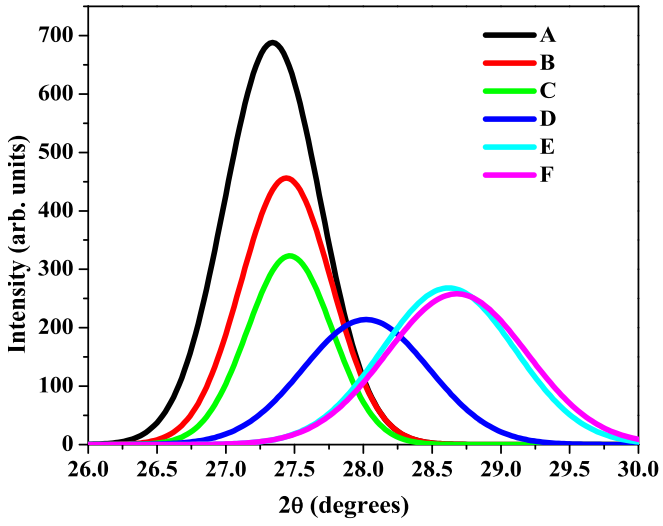

Fig.4. The most prominent GAXRD peak analysis.

Table 2
Structural parameters obtained from the preferential peak orientation.

Sample *ID*	2θ(°)	Peak height (arb. units)	β (rad)	Crystallite size (nm)
A	27.34	704	0.72	11.9
B	27.44	456	0.78	11.0
C	27.47	323	0.83	10.3
D	28.02	214	1.08	7.9
E	28.50	268	1.14	7.5
F	28.56	258	1.20	7.1

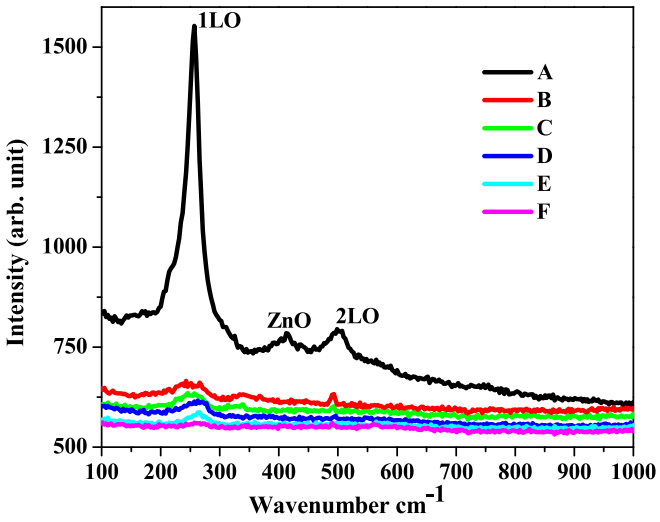

Fig.5. Raman scattering spectra of the ZnS_xSe_{1-x} ($0 \leq x \leq 1.0$) thin films.

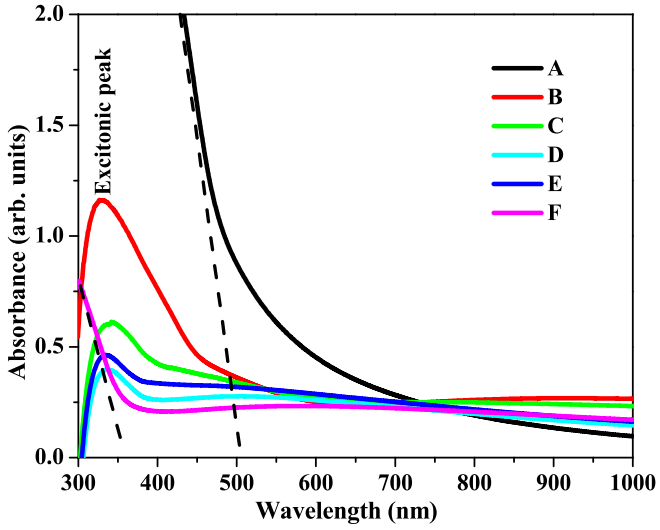

Fig.6. Absorption spectra of the ZnS_xSe_{1-x} ($0 \leq x \leq 1.0$) thin films.

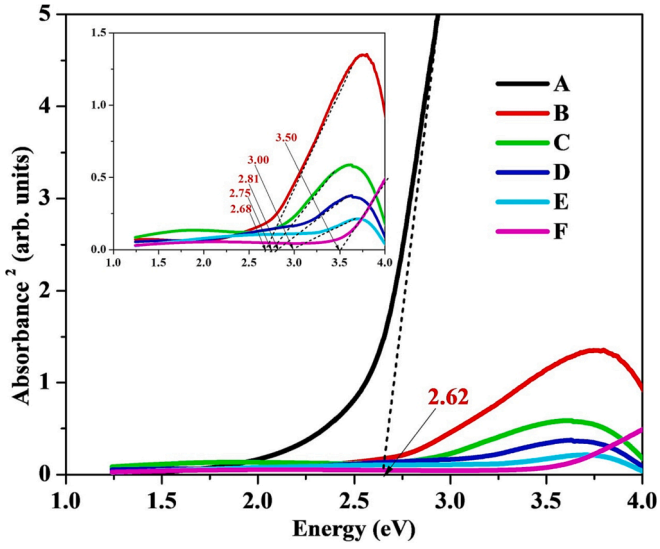

Fig.7. Estimation of the energy bandgap of the ZnS_xSe_{1-x} thin films.

Table 3
Energy bandgap of the ZnS_xSe_{1-x} thin films.

Sample *ID*	A	B	C	D	E	F
Bandgap (eV)	2.62	2.65	2.75	2.81	3.00	3.50

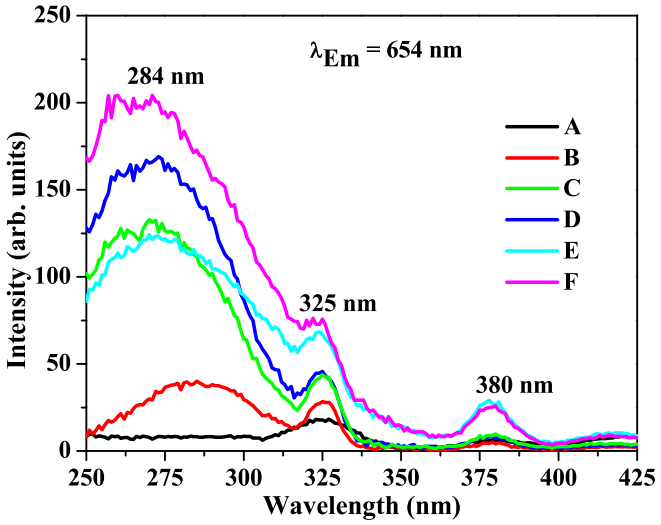

Fig.8. PL excitation spectra of the ZnS_xSe_{1-x} thin films.

freshly prepared Na_2SeSO_3 in a 100 mL beaker. The resulting mixture was stirred thoroughly to obtain a uniform solution and the pH was measured to be 10.8 using a pH meter. It should be understood here that the pH of the solution was obtained to be 10.8 without adding any other chemical to adjust it. Then the cleaned substrate was vertically immersed in the solution bath and the deposition was carried out at 80 °C under UV (50 W, 230 V) illumination. The deposition lasted for 2 h under gently and continuous stirring to maintain homogeneity of the solution. The process of PCBD involves the dissociation of Zn^{2+} ions from the complex reaction between $Zn(CH_3COO)_2$ and $N_2H_4{\cdot}H_2O$ in the solution bath then Na_2SeSO_3 absorbed the UV light and released solvated electrons and Se ions. The released Se^{2-} ions reacted with the complexed Zn^{2+} ions, which resulted to precipitation of ZnSe on the substrate. These processes are summarized in equations 1–3 (Hile et al., 2020).

$$Zn(CH_3COO)_2 + 2(N_2H_4.H_2O) \rightarrow [Zn(NH_3)_4]^{2+} + 2CH_3COO^- + O_2 \quad (1)$$

$$Na_2SeSO_3 + h\nu \rightarrow Na_2SO_3 + Se^{2-} \quad (2)$$

$$[Zn(NH_3)_4]^{2+} + Se^{2-} + h\nu \rightarrow ZnSe\downarrow + 4NH_3\uparrow \quad (3)$$

The excited electrons were used to increase the kinetic energy and hence the interdifussion of the absorbing particles (Remadevi and Dhanya, 2011).

The same procedure was employed for the deposition of the other samples but with the addition of different concentration of CH_4N_2S as the source of sulfur. For each value of x, there is a corresponding change in the value of selenium according to the matrix ZnS_xSe_{1-x}. With this arrangement, six samples of ZnS_xSe_{1-x} thin films were deposited and labelled A, B, C, D, E, F, respectively corresponding to 0, 0.1, 0.3, 0.5, 0.8 and 1.0 M of CH_4N_2S. All the deposited thin films were annealed in an open-air furnace at 250 °C for 3 h and allowed to cool naturally before characterization.

2.2. Materials characterization

The structural investigations of the deposited films were carried out

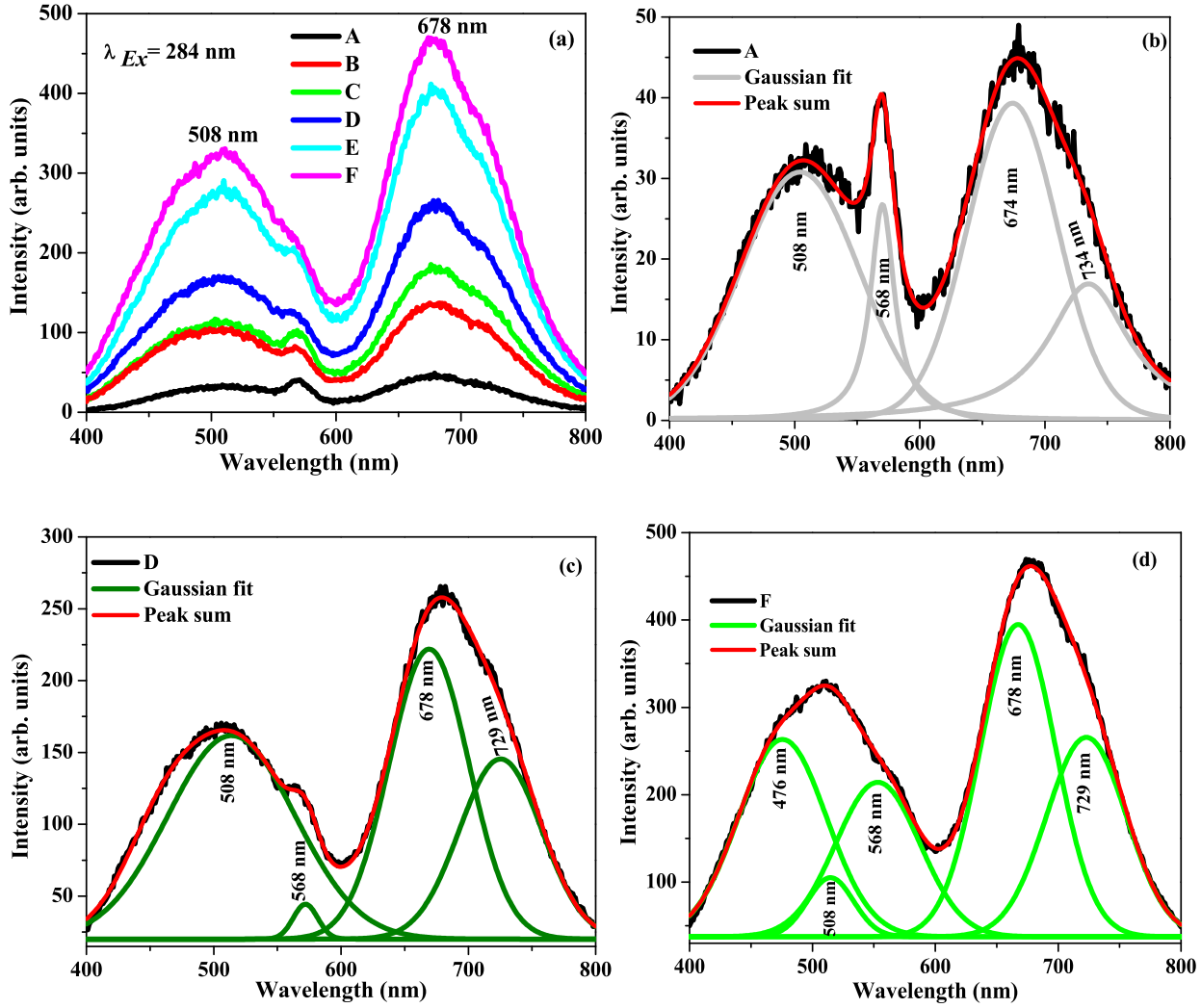

Fig.9. (a) Photoluminescence emission spectra of the ZnS_xSe_{1-x} thin films excited at 284 nm, (b) – (d) the deconvolution of samples A, D and F, respectively.

using a Rigaku smatlab glancing angle X-ray diffractometer (GAXRD) at a fixed wavelength of Cu kα = 0.1540 nm and at an angle of 1 degree. Optical vibrational modes on the thin films were analyzed at room temperature using WITech confocal Raman microscopy, while Joel JSM-7800F field emission scanning microscope (FESEM) was used for morphology characterization. The FESEM was attached with an Oxford energy dispersive X-ray (EDX) spectrometer that was used to evaluate the elementary composition of the thin films. The Shimadzu UV = 1700 UV–vis spectrometer was used for the optical analysis at room temperature in the wavelength range of 300 – 1000 nm. The luminescence properties were analyzed using a Varian Cary Eclipse fluorescence spectrophotometer with an inbuilt 150 W Xenon lamp.

3. 3.0 results and discussion

3.1. Energy dispersive X-ray spectroscopy (EDX) spectra

Fig. 1 shows the selected EDX spectra of the ZnS_xSe_{1-x} thin films of samples A, B, E and F. It can be seen in the spectrographs that all the expected elements are present in the samples. The weight percentages of these elements as well as the nominal chemical composition ($0 \leq x \leq 1.0$) of S are presented in Table 1. The other elements (i.e., O, Si, Na, Ca, Mg, and Al) detected which are not part of the ZnS_xSe_{1-x} are components of the glass substrates used while C is the carbon coding used during sample preparation for the EDX measurement. Similar impurity elements coming from the soda-lime glass substrate have also been reported by Bakiyaraj *et al.* (Bakiyaraj and Dhanasekaran, 2013).

3.2. Morphology analysis

The top view FESEM images of the ZnS_xSe_{1-x} ($0 \leq x \leq 1.0$) thin films are shown in Fig. 2. The sample A ($x = 0$) shows homogeneous nanoflake-like nanostructures that are evenly distributed and well covered the substrate. This morphology is similar and very consistent with our previous reports on pure ZnSe (Kumaresan et al., 2002; Hile et al., 2020). The introduction of S (from sample *B*) into the ZnSe matrix resulted into a change of morphology from the nanoflake-like to an agglomeration of spherical nanoparticles. The agglomeration becomes dispersed as the S content increased ($x = 0.23 – 1.0$) and the thin film's surface equally gets smoother yet evenly distributed on the substrate. The change in morphology with the addition of S can be attributed to the difference in ionic radii of Se (1.98 \AA) and S (1.84 Å) ions (Dimitrievska et al., 2016). Similar observation was earlier reported by Liu *et al.* (Liu et al., 2013) and they ascribed the behavior to the reaction mechanism between the ZnSe and ZnS.

3.3. Structural studies

The GAXRD patterns of the ZnS_xSe_{1-x} ($0 \leq x \leq 1.0$) thin films are shown in Fig. 3. The diffraction patterns of the thin films sample A

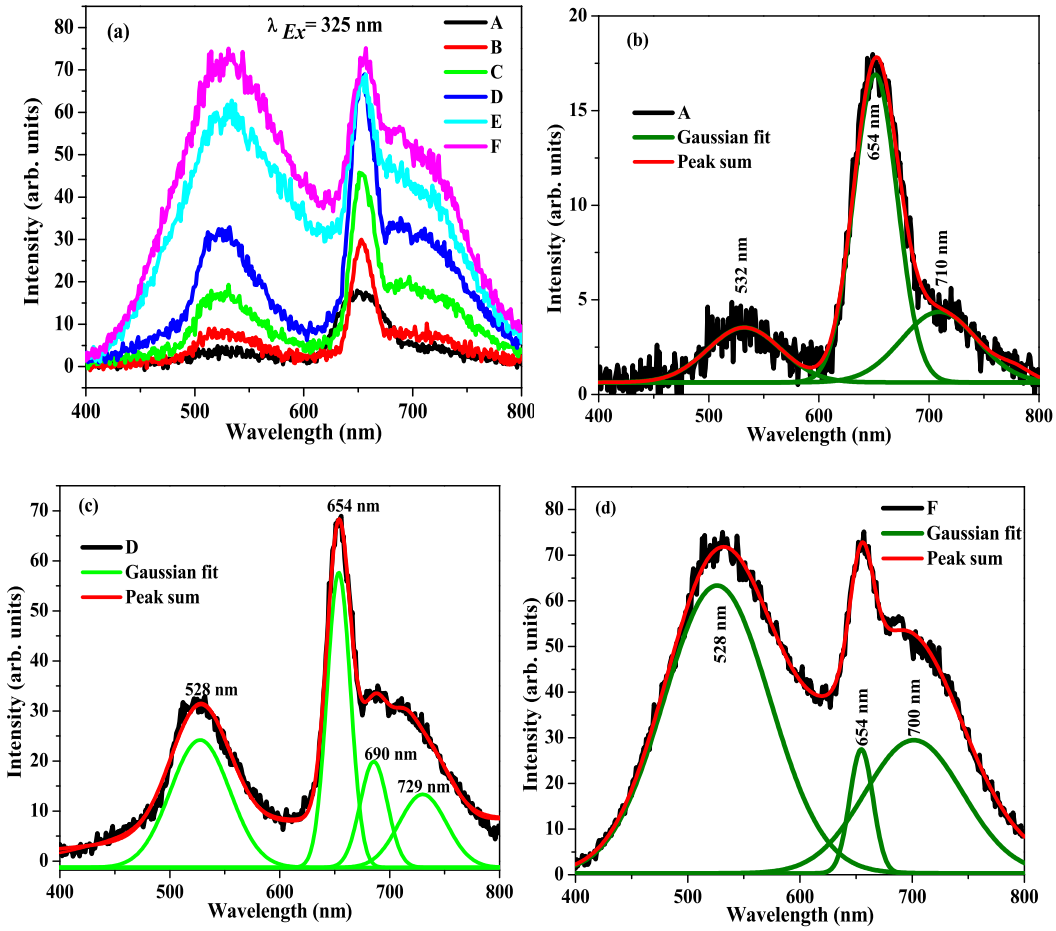

Fig.10. (a). Photoluminescence emission spectra of the ZnS_xSe_{1-x} thin films excited at 325 nm, (b) – (d) the deconvolution of samples A, D and F, respectively.

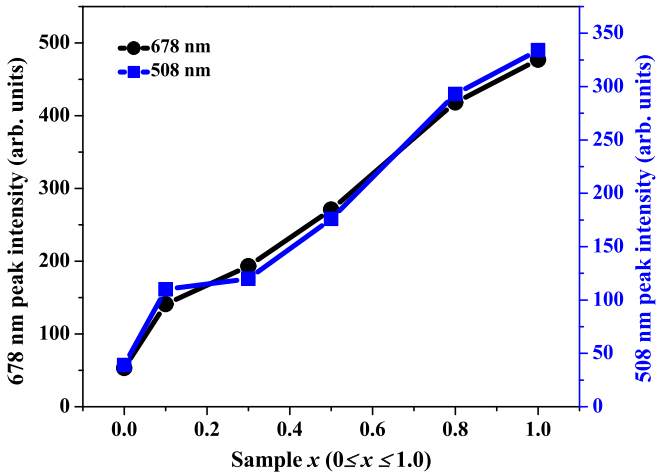

Fig.11. PL emission intensity as a function of x for the ZnS_xSe_{1-x} ($0 \leq x \leq 1.0$) thin films.

($CH_4N_2S = 0$) exhibit ZnSe peaks at the 2θ values of 25.96, 27.42, 29.26, 37.97, 45.48, 49.50 and 53.79°. Comparing the peaks positions with the standard values confirmed that the films are of hexagonal phase corresponding to the (100), (002), (101), (102), (110), (103) and (112) planes, respectively, according to the JCPDS card no: 15–0105. At sample F ($x = 1$, ZnS), a cubic structure appeared with a preferential orientation along the (111) plane corresponding to $2\theta = 28.56°$ matching well with JCPDS no: 05–0566. The identified peaks gradually changed positions, reduced in height, and broaden as x is increased. These observed changes could be traced to the structural transformation from hexagonal ZnSe to cubic ZnS as the amount of x was increased. The zoomed version of the (002) and (111) diffraction peaks of the ZnSe and ZnS, respectively, are presented in Fig. 4. The predominant peaks are observed to shift to higher 2θ values. Generally, these peaks height decreases while the peaks broadening increases with an increase in x and this is due to the replacement of Se by S in the ZnS_xSe_{1-x} matrix. The peak heights and broadening are presented in Table 2. Patil *et al.* (Patil et al., 2018) deposited ZnS_xSe_{1-x} thin films via the spray pyrolysis method and observed a similar behavior of structural changes. The crystallite sizes were estimated from the respective (002) and (111) diffraction peaks for the ZnSe and ZnS using the Scherrer-Debye relation (Patil et al., 2018). The estimated crystallite sizes are presented in Table 2. The crystallite size decreased linearly with increase in x values and this can be ascribed to an increase in the peak broadening.

3.4. Raman scattering

The vibrational properties of the ZnS_xSe_{1-x} ($0 \leq x \leq 1.0$) thin films were investigated using Raman scattering at excitation wavelength of 532 nm and the spectra is shown in Fig. 5. Three vibrational phonon mode peaks are located at 256, 412 and 499 cm^{-1} for sample A. The peaks at 256 and 499 cm^{-1} are the fundamental first longitudinal optic (1LO) and second order longitudinal optic (2LO) phonon mode peaks of ZnSe, respectively (Zhang et al., 2016; Tabar et al., 2018), while the peak located at 412 cm^{-1} can be ascribed to higher order combination bands of ZnO which arise from the open air annealing effect. For all the other samples, only the 1LO and 2LO peaks are present. These RAMAN

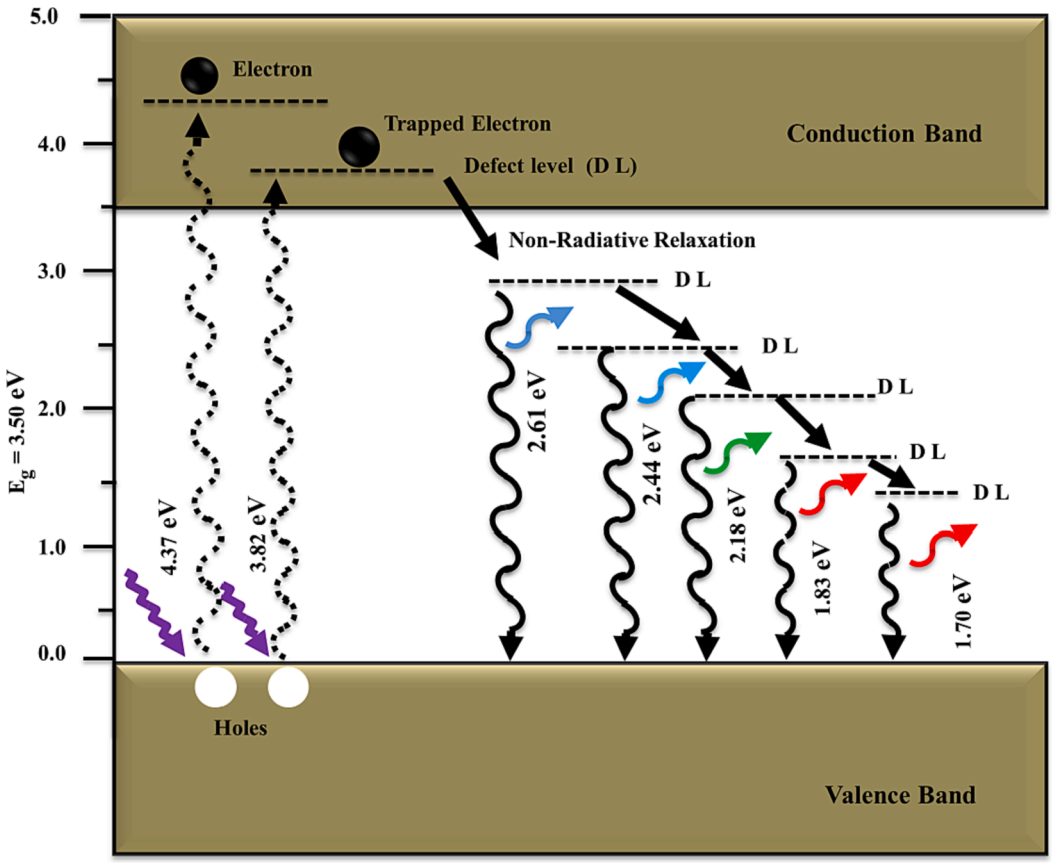

Fig.12. The proposed excitation and emission pathway mechanism on ZnS_xSe_{1-x} ($0 \leq x \leq 1.0$) thin films.

Table 4
CIE coordinates of the ZnS_xSe_{1-x} ($0 \leq x \leq 1.0$) thin films.

Sample *ID*	A	B	C	D	E	F
x coordinate	0.478	0.405	0.382	0.367	0.362	0.3589
y coordinate	0.397	0.472	0.471	0.475	0.454	0.453

peak intensities decrease with an increase in *x*. This is due to the very weak Raman scattering efficiency of the ZnSSe semiconductor structure caused by weak photon-matter interaction under standard excitation (532 nm) (Dimitrievska et al., 2016). Tabar *et al.* (Tabar et al., 2018) alleged that such changes can add stress on the structure of the nano-material leading to changes in the energy bandgap.

3.5. Optical properties

3.5.1. Uv–visible spectroscopy studies

The optical absorbance of the ZnS_xSe_{1-x} thin films deposited on the glass substrates is shown in Fig. 6. The absorption edges are observed to lie approximately between 350 and 500 nm. These bands are typical absorption edges for the ZnS (Wei et al., 2013) and ZnSe (Al-Kuhaili et al., 2013), respectively. It is clear that the absorption edge moved from sample A (ZnSe) to lower wavelengths as the *x* values were increased. This blue shift which can be ascribed to the decrease in crystallite size (Hile et al., 2020) is a clear indication that energy bandgap can be tuned with different permutation of *x* in the ZnS_xSe_{1-x} matrix. There is an excitonic peak at around 342 nm on samples B -E, which is very close to the known ZnS band-to-band and this is attributed to the more Se atoms being replaced by S atoms, which have different ionic radius.

The energy bandgap plots shown in Fig. 7 were obtained from the graph of the square of absorbance against photo energy (eV) as described in Ref. (Olusola et al., 2015; Echendu et al., 2017; Abdul-Manaf et al., 2015). The bandgap values obtained are presented in Table 3. The bandgap values for samples A and F are comparable to the typical bulk values of the ZnSe (2.67 eV) (Xie et al., 2017) and ZnS (3.50 eV) (Zein and Alghoraibi, 2019). The values of 2.68 – 3.00 eV are close to those reported by Nandkishor *et al.* (Patil et al., 2018) for ZnS_xSe_{1-x} compound. The inset in Fig. 7 is the zoom version of the samples except the sample A. It can be noted that the bandgap increased steadily with increase in *x* and the thin films gradually changed from the wurtzite ZnSe to cubic ZnS as seen in the GAXRD analysis. Valeev *et al.* (Valeev et al., 2015) varied the Se and S ion concentration from 0.36 to 0.73 and the bandgap changes between 2.25 and 3.00 eV. However, no change in the structure of the thin films was observed as all the samples remained of cubic structure despite been deposited on different substrates materials (Valeev et al., 2015). The increase on the bandgap with an increase in *x* while the crystallite sizes was decreased, and phase transformation, can be attributed to reduction in bond distance as more S atoms with smaller atomic (0.88 Å) radius replaced Se (1.03 Å) in ZnS_xSe_{1-x} compound (Clementi et al., 1967; Valeev et al., 2015).

3.5.2. Photoluminescence (PL) studies

Room temperature PL excitation spectra of the ZnS_xSe_{1-x} ($0 \leq x \leq 1.0$) thin films are shown in Fig. 8. The excitation spectra were carried out while monitoring emission at a wavelength of 654 nm. The sample A shows two excitation peaks around 325 and 380 nm while all the other samples revealed three excitation peaks located around 284, 325 and 380 nm. The peak at 284 nm may be due to Se vacancy as a result of the introduction of S. It can be seen that as the S content increased, the 284 nm peak intensity increased (Fig. 8). The peak at 325 nm is ascribed to near band transition in ZnSe while that at 380 nm is due to defect levels in ZnS_xSe_{1-x} (Kumaresan et al., 2002).

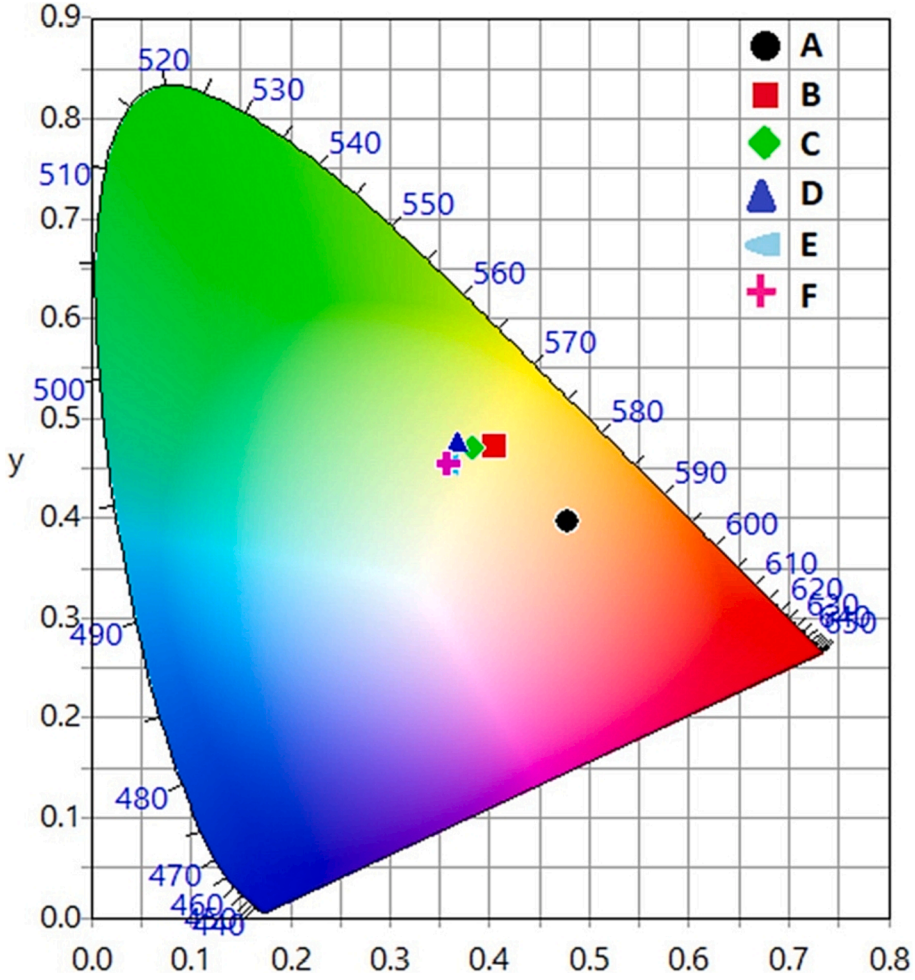

Fig.13. CIE color chromaticity diagram of the ZnS_xSe_{1-x} ($0 \leq x \leq 1.0$) thin films.

In order to study the PL emissions of the ZnS_xSe_{1-x} ($0 \leq x \leq 1.0$) thin films, the samples were excited using the wavelengths of 284 and 325 nm separately and the spectra are presented in Fig. 9 (a) and Fig. 10 (a), respectively. The 284 nm emission spectra (Fig. 9 (a)) revealed two broad asymmetric bands with peaks located around 508 and 678 nm. The deconvolution of the sample A illustrated in Fig. 9 (b) has shown four peaks located at 508, 568, 674 and 734 nm. The emission peaks at 508, 674 and 734 nm are attributed to different surface states in ZnSe, which could arise from Zn vacancies and non-stoichiometric emission (Miya et al., 2022; Hile et al., 2021) while the 568 nm emission peak is attributed to second order emission arising from the 284 nm excitation wavelength.

The deconvolution of the sample D ($x = 0.30$) is shown in Fig. 9 (c) with peaks at 508, 568, 678 and 729 nm. Fig. 9 (d) depicts the emission spectrum of the sample F ($x = 1.0$) with deconvoluted peaks at 476, 508, 568, 678 and 729 nm. For the 476 nm peak, a similar blue emission peak has been reported by Jrad *et al.* (Jrad et al., 2015) on ZnS nanostructure material and it was associated with Zn interstitial.

The emission spectra from the 325 nm excitation (illustrated in Fig. 10 (a)) revealed three main emission peaks located at 532, 654 and 710 nm. This is clearly seen in the deconvolution of the $x = 0$ (ZnSe) sample shown in Fig. 10(b). The 532 and 710 nm emission peaks have been earlier reported and ascribed to defect levels arising from non-stoichiometric defects, Zn vacancies and interstitial states in ZnSe (Hile et al., 2020), respectively. The 654 nm peak is attributed to interstitial states in ZnSe.

The deconvolution of the sample D is shown in Fig. 10 (c). The results revealed that there are four emission peaks located at 532, 654, 690, and 729 nm. The emission peaks at 532, 654, nm are assigned to S^{2-} ions vacancies and interstitial, respectively (Jrad et al., 2015), while that at 690 nm is due to Zn vacancies in ZnS matrix. However, the peak at 729 nm can be attributed to the presence of S^{2-} ions in the ZnS_xSe_{1-x} compound. Fig. 10 (d) shows the deconvolution of the sample F (ZnS), which revealed that there are three emission peaks located at 532, 654, and 700 nm. These emission peaks are respectively attributed to the S^{2-} ions vacancies, interstitial and Zn vacancies (Patel et al., 2017). The emission intensity for the 508 and the 678 nm as a function of the x is shown in Fig. 11 and the results revealed a linear relationship. The increased emission intensity is consistent with the bandgap increase as x changes from 0 to 1. This increase is caused by the natural defects in the host material. Increasing doping concentrations enhances the localized defect states leading to increased peak intensity, energy bandgap and decrease in the crystallite size (Patel et al., 2017). This process may be caused by the shrinking of the ZnSe with larger lattice constant (5.669 Å) to ZnS with smaller lattice constant (5.406 Å) (Song et al., 2000). The proposed observed emission pathways are shown in Fig. 12.

The self-activated emissions arising from defect levels such as vacancies and interstitials are known to create traps states within the bandgap (between the top of the valence band and the bottom of the conduction band) (Jobzari et al., 2019). In order to explain the dynamics behind the PL excitation and emission pathways of the deposited ZnS_xSe_{1-x} thin films, it is necessary to propose a schematic band diagram to demonstrate all of the associated processes. The proposed PL excitation and emission pathways for the ZnS_xSe_{1-x} ($0 \leq x \leq 1.0$) thin films are illustrated in Fig. 12. Considering the fact that the bulk energy bandgap of ZnS (3.50 eV) (Abdallah et al., 2019) and ZnSe (2.70 eV)

(Thirumavalavan et al., 2016) are different, when the electrons in the valence band are excited by high UV energy 4.37 eV (284 nm) or 3.82 eV (325 nm) into the conduction band, it is possible that excited electrons may be trapped either in the Conduction band of ZnS or that of ZnSe. These serve as defect state levels for trapping of the excited electrons. Since electrons are always short-lived in excited state, they will be de-excited by non-radiative relaxation through different channels (as shown in Fig. 12) and may be trapped by other defect states. In these states, the electrons are further de-excited by radiative decay to recombine with the holes in the valence band. Due to the presence of different defect states, the de-excited electrons emit different energies or colours in the visible range. The visible range emissions are commonly associated with either intrinsic or extrinsic deep level defects such as Zn^{2+} or S^{2-} ions vacancies and interstitials (Motlounga et al., 2018) as earlier mentioned.

3.5.3. Color analysis

The colour analysis of the ZnS_xSe_{1-x} ($0 \leq x \leq 1.0$) thin films was carried out using the CIE 1931 chromaticity coordinates calculator software. The software was used to determine the (x: y) coordinates and the values are presented in Table 4. The plot of the coordinates on the chromaticity diagram illustrated in Fig. 13 shows that the sample $x = 0$ emits a reddish colour which was tuned to yellowish-green x was varied from 0 to 1.0. This tunable property of the deposited films with variation in x shows that the thin films can gain useful applications in light emitting technology.

3.6. Conclusion

In this study, ZnS_xSe_{1-x} ($0 \leq x \leq 1.0$) thin films were deposited from different S^{2-} ions concentrations, $x = 0$, 0.12, 0.23, 0.3, 0.7 and 1 using PCBD technique. The PCBD technique was used to deposit ZnS_xSe_{1-x} thin films due to the advantages it has over Non-PCBD and other deposition techniques such as effective deposition of heterogenous thin films, efficient convertion of the reactants to the required product and higher deposition rate.The effect of varying x on the ZnS_xSe_{1-x} structural analyses revealed a gradual change from polycrystalline wurtzite ZnSe structure to cubic ZnS as x values were increased. Although no peaks were observed from the vibration phonon modes due to S^{2-} ions, the intensity of the observed peaks which were attributed to the longitudinal optic modes of ZnSe were found to decrease with increase in x concentration. The thin films morphology also changed from nanoflakes when $x = 0$ to spherical nanoparticles as x tends to 1.0. The presence of all the expected elements was confirmed by the EDX analysis. The energy bandgap of the deposited thin films was tuned from 2. 67 – 3.50 eV as x concentration was varied from $0 - 1.0$, respectively. The PL excitation revealed three peaks located at 284, 325 and 380 nm and two broad emission bands with several embedded peaks, which are all ascribed to intrinsic and extrinsic deep level defects such as non-stoichiometric defects, Zn^{2+} or S^{2-} ions vacancies and interstitials. The effect of the increased x concentration from 0 to 1.0 was evident on the PL peaks intensities. The CIE results revealed that the emission colors were tuned from red to yellowish-green as x concentration changes. The tunable optical properties of the ZnS_xSe_{1-x} compound can afford the material to a variety of optoelectronic applications such as light emitting diodes and photo scintillators.

Declaration of competing interest

The authors declare that they have no known competing financial interests or personal relationships that could have appeared to influence the work reported in this paper.

Data availability

No data was used for the research described in the article.

Acknowledgments

The authors would like to acknowledge the National Research Foundation, UID: 99224, the University of the Free State, the South African Research Chairs Initiative of the Department of Science and Technology (DST), the National Research Fund (NRF) (Grant 84415) and NRF incentive funding for rated researchers (IPRR) (Grant No: 126914) for their financial support.

References

Abdallah, B., Kakhia, M., Alkafri, N., 2019. Investigation of ZnS Nanotubes Films: Morphological, Structural and Optical Properties. J. Nano Res. 60, 142–153. https://doi.org/10.4028/www.scientific.net/JNanoR.60.142.

N.A. Abdul-Manaf, A.R. Weerasinghe, O.K. Echendu, I.M. Dharmadasa Electro-plating and characterisation of cadmium sulphide thin films using ammonium thiosulphate as the sulphur source, J. Mater. Sci. Mater. Electron. 26 (2015) 2418–2429, DOI 10.1007/s10854-015-2700-5.

Al-Kuhaili, M.F., Kayani, A., Durrani, S.M.A., Bakhtiari, I.A., Haider, M.B., 2013. Band gap engineering of ZnSe thin films through alloying with cadmium telluride. ACS Appl. Mater. Interfaces 5, 5366–5372.

Bakiyaraj, G., Dhanasekaran, R., 2013. Syntnihesis and characterization of flower-like ZnSe nanostructured thin films by chemical bath deposition (CBD) method. Appl. Nanosci. 3, 125–131. https://doi.org/10.1007/s13204-012-0075-y.

Clementi, E., Raimondi, D.L., Reinhardt, W.P., 1967. Atomic Screening Constants from SCF Functions. II. Atoms with 37 to 86 Electrons. J. Chem. Phys. 47, 1300–1307. https://doi.org/10.1063/1.1712084.

Dimitrievska, M., Xie, H., Jackson, A.J., Fontané, X., Espíndola-Rodríguez, M., Saucedo, E., Pérez-Rodríguez, A., Walsh, A., Izquierdo-Roca, V., 2016. Resonant Raman scattering of ZnS_xSe_{1-x} solid solutions: the role of S and Se electronic states. PCCP 18 (11), 7632–7640. https://doi.org/10.1039/c5cp04498g.

Echendu, O.K., Dejene, F.B., Dharmadasa, I.M., Eze, F.C., 2017. Characteristics of Nanocrystallite-CdS Produced by Low-Cost Electrochemical Technique for Thin Film Photovoltaic Application: The Influence of Deposition Voltage. Inter J. Photoenergy 3989432, 1–13. https://doi.org/10.1155/2017/3989432.

Hile, D.D., Swart, H.C., Motloung, S.V., Motaung, T.E., Egbo, K.O., Koao, L.F., 2019. Comparative study of photo- and non-photo-assisted chemical bath deposition of Zinc Selenide thin films using different volumes of hydrazine hydrate. Superlattice. Microst. 134, 106222 https://doi.org/10.1016/j.spmi.2019.106222.

Hile, D.D., Swart, H.C., Motloung, S.V., Kroon, R.E., Egbo, K.O., Koao, L.F., 2020. The effect of annealing time on zinc selenide thin films deposited by photo-assisted chemical bath deposition. J. Phys. Chem. Solid 140, 109381. https://doi.org/10.1016/j.jpcs.2020.109381.

Hile, D.D., Swart, H.C., Motloung, S.V., Motaung, T.E., Kroon, R.E., Egbo, K.O., Pawade, V.B., Koao, L.F., 2021. Synthesis and characterization of europium doped zinc selenide thin films prepared by photo-assisted chemical bath technique for luminescence application. Mater. Chem. Phys. 262, 124303 https://doi.org/10.1016/j.matchemphys.2021.124303.

Huentupil, Y., Cabello-guzman, G., Chornik, B., Arancibia, R., Buono-core, G.E., 2019. Photochemical deposition, characterization and optical properties of thin films of ThO2. Polyhedron 157, 225–231. https://doi.org/10.1016/j.poly.2018.10.023.

Jobzari, H.G., Iranmanesh, P., Sabet, M., Saeednia, S., 2019. Effect of synthesis method and chemical reagents on the structural parameters, particle size, and optical and photoluminescence properties of ZnS nanostructures. Lumin 1–10. https://doi.org/10.1002/bio.3650.

Jrad, A., Nasr, T.B., Turki-Kamoun, N., 2015. Study of structural, optical and photoluminescence properties of indium-doped zinc sulfide thin films for optoelectronic applications. Optical Mater 50, 128–133. https://doi.org/10.1016/j.optmat.2015.10.011.

Korepanov, V.I., Chan, S.Y., Hsu, H.C., Hamaguchi, H., 2019. Phonon confinement and size effect in Raman spectra of ZnO nanoparticles. Heliyon 5, e01222.

Kulkarni, R., Rondiya, S., Pawbake, A., Waykar, R., Jadhavar, A., Jadkar, V., Bhorde, A., Date, A., Pathan, H., Jadkar, S., 2017. Structural and optical properties of CdTe thin films deposited using RF magnetron sputtering. Energy Procedia 110, 188–195. https://doi.org/10.1016/j.egypro.2017.03.126.

Kumaresan, R., Ichimura, M., Arai, E., 2002. Photochemical deposition of ZnSe polycrystalline thin films and their characterization. Thin Solid Films 414, 25–30. https://doi.org/10.1016/S0040-6090(02)00450-9.

Z.R. Lindsey, M.W. Rhoades, V.V. Fedorov, S.B. Mirov, R.P. Camata,. Pulsed Laser Deposition of Relaxed ZnS_xSe_{1-x} Thin Films for Waveguiding Applications in Mid-IR Active Cr2+: ZnSe Multilayered Structures. In Advanced Solid State Lasers (pp. AM5A-19), *Opt. Soc. Am.* (2016, October), Doi: 10.1364/ASSL.2016.AM5A.19.

Liu, J., Wei, A.X., Zhuang, M.X., Zhao, Y., 2013. Investigation of the ZnS_xSe_{1-x} thin films prepared by chemical bath deposition. J. Mater. Sci. Mater. Electron. 24 (4), 1348–1353. https://doi.org/10.1007/s10854-012-0932-1.

Miya, L.A., Motloung, S.V., Motaung, T.E., Swart, H.C., Hile, D.D., Koao, L.F., 2022. Study of the structural, morphological and optical properties of ZnSe doped with Yb^{3+}. Mater Today Com 33, 104677. https://doi.org/10.1016/j.mtcomm.2022.104677.

Motlounga, S.V., Kumari, P., Koao, L.F., Motaung, T.E., Hlatshwayo, T.T., Mochane, M.J., 2018. Effects of annealing time on the structure and optical properties of $ZnAl_2O_4$/ZnO prepared via citrate sol-gel process. Mater Today Com 14, 294–301. https://doi.org/10.1016/j.mtcomm.2018.02.004.

Olusola, O.I., Echendu, O.K., Dharmadasa, I.M., 2015. Development of CdSe thin films for application in electronic devices. J. Mater. Sci. Mater. Electron. 26, 1066–1076. https://doi.org/10.1007/s10854-014-2506-x.

Park, J.Y., Jeon, E.J., Choa, Y.H., Kim, B.S., 2019. Optical and structural properties of ZnSe quantum dot with europium. J. Lumin. 208, 145–149. https://doi.org/10.1016/j.jlumin.2018.12.018.

Patel, P.C., Ghosh, S., Srivastava, P.C., 2017. Effect of impurity concentration on optical and magnetic properties in ZnS: Cu nanoparticles. Physica E 93, 148–152. https://doi.org/10.1016/j.physe.2017.06.009.

Patil, N.M., Nilange, S.G., Yadav, A.A., 2018. Growth and characterization of ZnS_xSe_{1-x} thin films deposited by spray Pyrolysis. Thin Solid Films 664, 19–26. https://doi.org/10.1016/j.tsf.2018.08.018.

Popa, M., 2016. The optical properties of ZnS_xSe_{1-x} thin films deposited by the quasi-closed volume technique. Rom Rep. Phys. 68 (4), 1495–1505.

Ray, S., Barman, B., Darshan, C., Tarafder, K., Bangera, K.V., 2022. ZnS_xSe_{1-x} thin films: A study into its tunable energy band gap property using an experimental and theoretical approach. Sol. Eng. 240, 140–146. https://doi.org/10.1016/j.solener.2022.05.019.

Remadevi, T.L., Dhanya, A.C., 2011. Photoassisted chemical deposition of nano crystalline ZnS thin films from aqueous alkaline bath. Arch Phys. Res. 2, 128–136.

Remadevi, T.L., Dhanya, A.C., Deepa, K., 2014. Photoassisted chemically deposited tin sulfide thin films based on two different chemical formulations. J. Electron. Mater. 43, 3984. https://doi.org/10.1007/s11664-014-3325-9.

Song, J.H., Sim, E.D., Baek, K.S., Chang, S.K., 2000. Optical properties of ZnSxSe1-x ($x < 0.18$) random and ordered alloys grown by metalorganic atomic layer epitaxy. J. Cryst. Growth 214 (215), 460–464.

Tabar, M.B., Elahi, S.M., Ghoranneviss, M., Yousefi, R., 2018. Controlled morphology of ZnSe nanostructures by varying Zn/Se molar ratio: the effects of different morphologies on optical properties and photocatalytic performance. Cryst. Eng. Comm. 20 (32), 4590–4599. https://doi.org/10.1039/c8ce00775f.

Thirumavalavan, S., Mani, K., Sagadevan, S., 2016. A study of structural, morphological, optical and electrical properties of Zinc Selenide (ZnSe) thin film. Mater. Today:. Proc. 3, 2305–2314. https://doi.org/10.1016/j.matpr.2016.04.141.

Valeev, R.G., Romanov, E.A., Vorobiev, V.L., Mukhgalin, V.V., Kriventsov, V.V., Chukavin, A.I., Robouch, B.V., 2015. Structure and properties of ZnS_xSe_{1-x} thin films deposited by thermal evaporation of ZnS and ZnSe powder mixtures. Mater. Res. Express 2, 025006. https://doi.org/10.1088/2053-1591/2/2/025006.

Wei, A., Liu, J., Zhuang, M., Zhao, Y., 2013. Preparation and characterization of ZnS thin films prepared by chemical bath deposition. Mater Sci Semicond Proc 16, 1478–1484. https://doi.org/10.1016/j.mssp.2013.03.016.

P. Xie, S. Xue, Y. Wang, Z. Gao, H. Feng, L. Li, D. Wu, L. Wang, Paul K. Chu, Morphology-controlled synthesis and electron field emission properties of ZnSe nanowalls, *RSC Adv*, 7 (2017) 10631, DOI: 10.1039/c6ra27541a.

Zein, R., Alghoraibi, I., 2019. Influence of Bath Temperature and Deposition Time on Topographical and Optical Properties of Nanoparticles ZnS Thin Films Synthesized by a Chemical Bath Deposition Method. J. Nanomater. 7541863, 1–13. https://doi.org/10.1155/2019/7541863.

Zhang, Q., Li, H., Ma, Y., Zhai, T., 2016. ZnSe nanostructures: Synthesis, properties and applications. Prog. Mater Sci. 83, 472. https://doi.org/10.1016/j.pmatsci.2016.07.005.